PAPER

An aerodynamic model for insect flapping wings in forward flight

IOP Publishing Bioinspir. Biomim. 12 (2017) 036004 https://doi.org/10.1088/1748-3190/aa640d

Bioinspiration & Biomimetics

RECEIVED
27 October 2016

REVISED
26 January 2017

ACCEPTED FOR PUBLICATION
2 March 2017

PUBLISHED
31 March 2017

PAPER

An aerodynamic model for insect flapping wings in forward flight

Jong-Seob Han[1], Jo Won Chang[2] and Jae-Hung Han[1]

[1] Department of Aerospace Engineering, Korea Advanced Institute of Science and Technology (KAIST), 291 Daehak-ro, Yuseong-gu, Daejeon, Republic of Korea
[2] Department of Aeronautical Science and Flight Operation, Korea Aerospace University, 76 Hanggongdaehak-ro, Goyang-city, Gyeonggi-do, Republic of Korea

E-mail: jaehunghan@kaist.ac.kr

Keywords: quasi-steady aerodynamic model, flapping wing, insect flight, advance ratio, forward flight

Abstract

This paper proposes a semi-empirical quasi-steady aerodynamic model of a flapping wing in forward flight. A total of 147 individual cases, which consisted of advance ratios J of 0 (hovering), 0.125, 0.25, 0.5, 0.75, 1 and ∞, and angles of attack α of -5 to 95° at intervals of 5°, were examined to extract the aerodynamic coefficients. The Polhamus leading-edge suction analogy and power functions were then employed to establish the aerodynamic model. In order to preserve the existing level of simplicity, K_P and K_V, the correction factors of the potential and vortex force models, were rebuilt as functions of J and α. The estimations were nearly identical to direct force/moment measurements which were obtained from both artificial and practical wingbeat motions of a hawkmoth. The model effectively compensated for the influences of J, particularly showing outstanding moment estimation capabilities. With this model, we found that using a lower value of α during the downstroke would be an effective strategy for generating adequate lift in forward flight. The rotational force and moment components had noticeable portions generating both thrust and counteract pitching moment during pronation. In the upstroke phase, the added mass component played a major role in generating thrust in forward flight. The proposed model would be useful for a better understanding of flight stability, control, and the dynamic characteristics of flapping wing flyers, and for designing flapping-wing micro air vehicles.

1. Introduction

Aerodynamic force augmentation mechanisms of flapping wings have been successfully revealed over the last few decades [1, 2]. Several vortex-dominated mechanisms, such as the delayed stall [3], Kramer effect [4], and wing-wake interaction [5] have been found, and numerous follow-up studies using numerical simulations and experiments have systematically confirmed the results [6–8]. Currently, a popular area of study is the aerodynamics of flapping wings in various configurations [9–11]. Many of these findings have become stepping stones to the development of various flapping wing aerodynamic models [12]. Although such models cannot reflect all aspects of the fluid physics, such as the surface friction or pressure disturbances caused by viscous and wake vortices near the field around the wings, their estimation performances with reasonable computing costs demonstrate their usefulness. These models have been broadly utilized for static/dynamic stability and flight control analyses of biological flyers as well as to determine the preliminary design parameters of flapping-wing micro air vehicles (FWMAVs) [13–18].

One typical example is the semi-empirical aerodynamic model announced by Sane and Dickinson [12]. They used a uniform stroke velocity with individual angles of attack to build a translational aerodynamic force model, i.e. $C_L(\alpha)$ and $C_D(\alpha)$. This work favorably compensated for the additional force due to the leading-edge vortex (LEV) attachment [3], which could not be formulated by the conventional approach [19]. In addition, they employed the Kutta–Joukowski theory and an analytic added mass model [20], expressed as functions of $C_F(\dot{\alpha})$ and $C_F(\ddot{\alpha})$, to predict forces which deviate from a quasi-steady state. By adding all of these factors, this model showed good agreement with the time-historical aerodynamic force acting on flapping wings, except for the instantaneous peak at the beginning of each wing stroke. As is well known, this exception is caused by the wing-wake interaction, which is now regarded as one of the types of unsteady phenomena [21, 22].

An analytical approach was derived by Ansari *et al* [23]. They classified aerodynamic mechanisms into the three major components of non-circulatory lift (added mass), circulatory lift, and unsteady circulatory lift (wake behavior). Mathematical expressions such as the Wagner, Loewy, and Kussner models were employed to describe the vortical behaviors. In addition, the Polhamus leading-edge suction analogy [24–26] was used to describe the contribution of the LEV (vortex lift). The aerodynamic lift using this model was in line with experimental results [5] within differences of ~9%. In 2007, Berman and Wang [27] derived a more generalized aerodynamic model that was based on the model of Andersen *et al* [28]. They took the viscous model into account to compensate for the low Re configuration and used the model to find energy-minimized wing kinematics. Taha *et al* [29] proposed the use of Duhamel's principle in an analytical model in order to consider the LEV contribution and the non-conventional lift curves. Their model showed fewer differences in the direct Navier–Stokes equation (DNS) results [30] than earlier models. More recently, Han *et al* [31] suggested an accurate pitching moment model that is critical to flight dynamic analyses. They investigated the behavior of the centers of pressure (CP) on a robotic wing model, showing that the quarter chord assumption (CP at $1/4c$) may result in an incorrect pitching moment prediction.

Although recent models give accurate force and moment estimations for flapping wings, they are still constrained by each condition of use, such as a wing planform, Reynolds number Re, aspect ratio AR, and advance ratio J. Among them, J should remain at zero in order to satisfy the hovering condition and to yield an acceptable estimation. The works by Lentink and Dickinson [32, 33] are typical examples of how J distorts the overall aerodynamic characteristics. They revealed that the fluidic stability of the LEV is governed by rotational force components, i.e. angular, centripetal and Coriolis accelerations, which are functions of the J and AR. Recent work by Han *et al* [34, 35] also found that AR and J led to remarkable changes in the LEV and consequent lift augmentation. According to their findings, a higher value of J can reduce by ~50% the aerodynamic performances of flapping wing [35].

Dickson and Dickinson [36] recognized that the direct implementation of the quasi-steady model [12] is not appropriate for forward flight. They defined the velocity ratio μ between the wing tip and forward flight speed and used it to revise the aerodynamic coefficients, which are in the form of quadratic functions of μ. With regard to FWMAVs, however, this remains questionable because their model focused on fruit flies, which have ultra-low Re values (~10^2). As numerous studies have indicated, the Re of flapping wings which exceeds ~10^3 induces distinctive aerodynamic characteristics. An intense spanwise flow [37], dual and multiple LEVs [38, 39], and a coherent system associated with LEV breakdowns [40, 41] are typical examples in the case of high Re (>10^3). Relatively weak viscous diffusion [42] and the consequent negligible portion of the viscous shear [43] are other features of a high Re. The revolving wing experiment conducted as part of their work [44] would also result in wake structures different from those formed by flapping wings [36]. These outcomes clearly suggest that the effects of J and a related compensation methodology for an aerodynamic model should be investigated such that accurate aerodynamic forces and moments can be determined.

In this study, we conduct direct force/moment measurements of a model wing moving forward at a relatively high Re and propose an extended aerodynamic model that can account for the effect of J. To this end, a high-precision scaled-up robotic manipulator [45] which is simultaneously controlled with a servo-driven towing tank is developed. The angle of attack α along with J were the variables of the present aerodynamic model, where J covered the maximum flight speeds of most insects [46, 47]. The present model will be helpful as it offers a better understanding of flight stability, control, and dynamics [48] for both flying insects and FWMAVs. It may also eventually be employed in the design of a bio-inspired FWMAV.

2. Materials and methods

Figure 1 describes the towing tank and depicts a scaled-up robotic model with three rotational degrees of freedom in the stroke angle ϕ^B, pitch angle θ^B, and deviation angle ψ^B at a single pivot, where the superscript B denotes the body-fixed frame. α is typically defined as the chord line angle from the direction of the inflow, and it served as one of the parameters in the present aerodynamic model (refer to appendix B for details). Instead of multiple bevel gears as employed in previous studies [5, 49, 50], we used a differential-type gearbox (BS-45T, Kyouiku Gear) as a power train. Because this gearbox has only one bevel gear at the end of each shaft, we could overcome the geometrical constraints of the robotic model and could achieve the shortest distance to the wing root from the pivot point, a more reasonable second moment of the wing area r_2, and kinematic similarity to living insects [51] (see the enlarged schematic in figure 1(a)). The excessively low tolerance of 1/4° guaranteed by the manufacturer allows for the precise control of arbitrary wing kinematics, and timing pulleys (GT2, MISUMI) suitable for positioning were mounted at the input shafts.

Figures 1(b) and (c) are schematics showing the servo-driven towing tank, which can be filled with up to four metric tons of water. A rack and pinion combination was equipped to drive the manipulator forward along the longitudinal direction. The lack gear has a length of 2.75 m and was installed across each side of the water tank. All of these servo motors were connected to a PC at a maximum baud rate of 2 Mbps

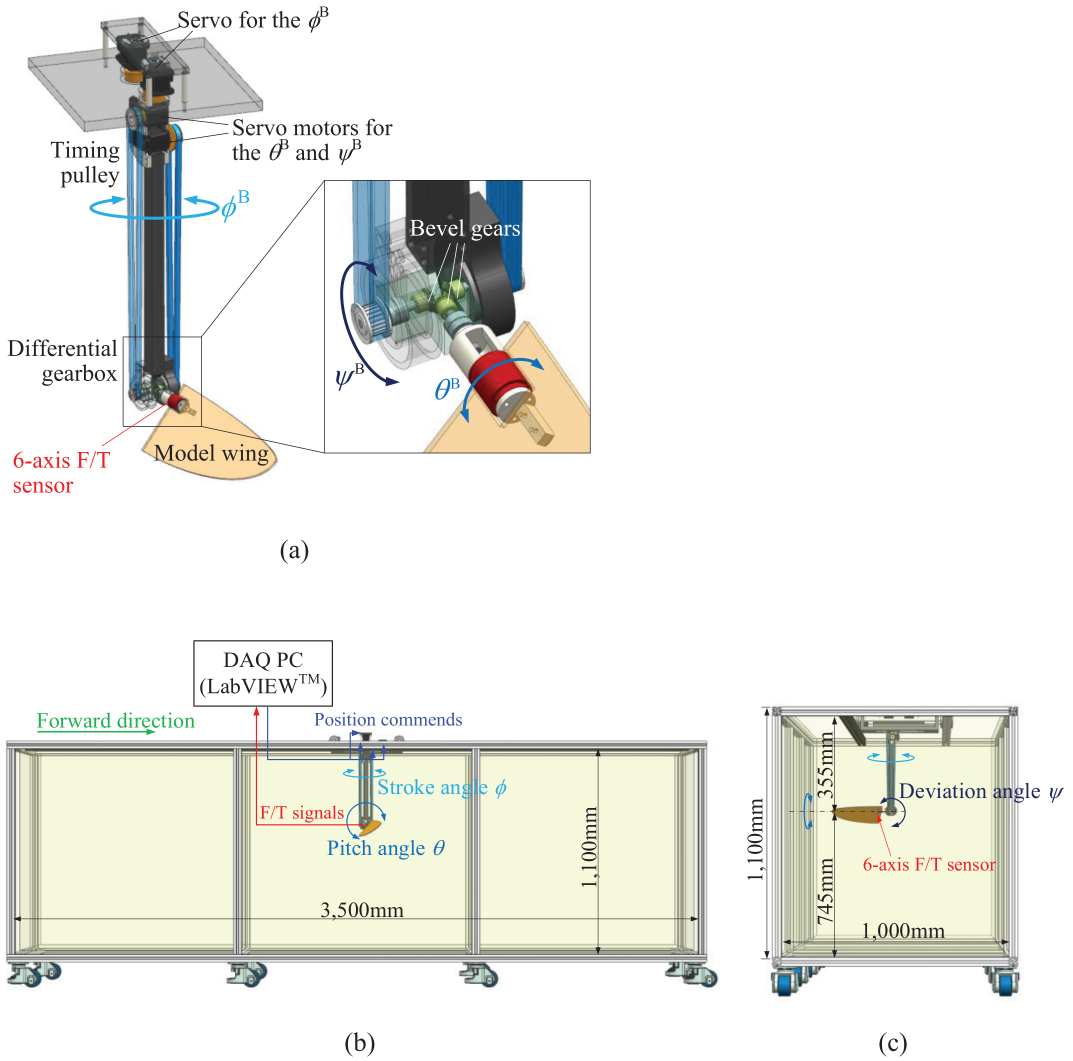

Figure 1. Experimental setup. (a) Schematic of the three-rotational DOF robotic manipulator. (b) Side view of the servo-driven towing tank. (c) Front view.

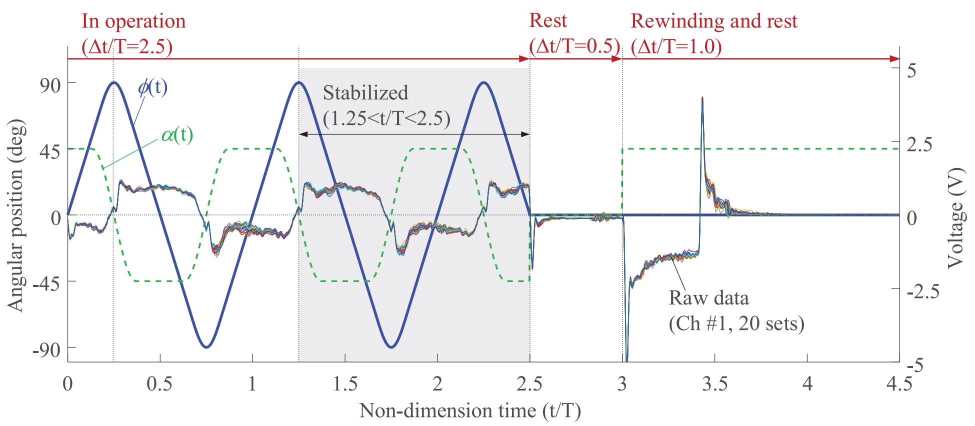

Figure 2. Temporal procedure for the force/moment measurement using the towing tank.

for simultaneous control. High-resolution encoders (1/4096°) installed in the motors (MX-28T, Robotis) enable precise positioning. An in-house code written in LabVIEW™ generated discrete position data arrays and updated the angular positions every 5 ms. This was enough to result in continuous wing motion.

The inverse Zimmerman wing planform [1], which consists of two quadratic curves close to the quarter chord, was employed. For sufficient rigidity, this wing model was made of a 3 mm thick transparent acrylic plate. Based on insect wings and on other fundamental studies indicating optimal AR values of ~3.0 [34],

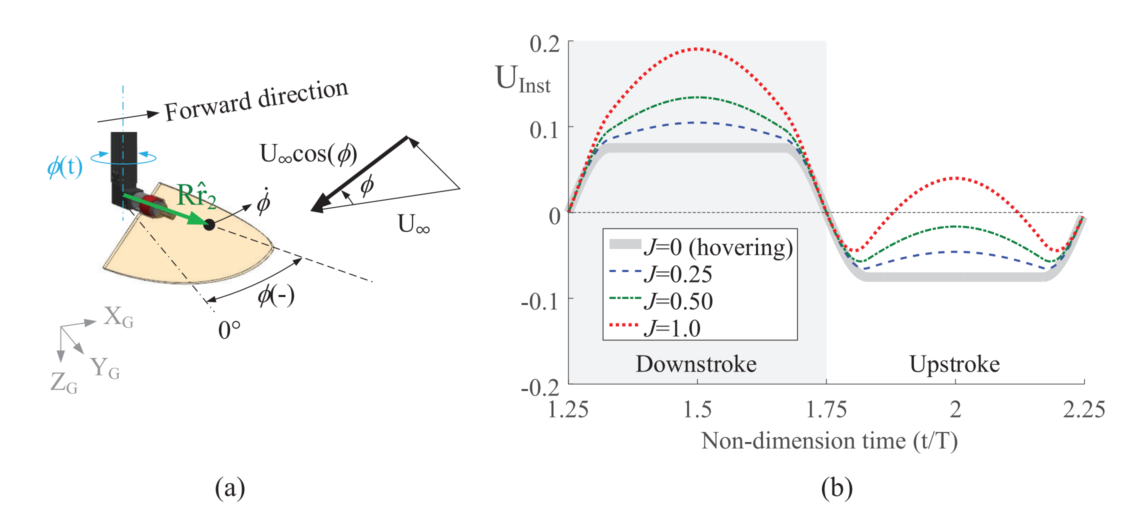

Figure 3. Definitions of the reference quantities and related motions. (a) A schematic of the wing in operation. (b) Instantaneous stroke velocity.

the AR and the spanwise length b were set as 3.0 and 250 mm, respectively. A small six-axis loadcell (Nano17 IP68, ATI Industrial Automation) with ranges of $\pm$25 N and $\pm$250 N mm was installed between the output shaft and the wing root with a margin of 0.2b; thus, the stroke axis was located 1.2b from the wingtip. As a result, the mean chord length $\bar{c}$ and the dimensionless second moment of the wing area $\hat{r}_2$ became 83.33 mm and 0.567, respectively, where the hat on r_2 denotes normalization by R (see appendix A for details). A DAQ board (PCI-6143, NI) supporting simultaneous sampling and holding was employed to acquire raw signals on six channels.

Figure 2 explains how the aerodynamic force and moment for non-zero J cases were obtained. We employed the prescribed time-historical angular motions shown in figure 2(a). While ψ^B was fixed at zero for the horizontal stroke plane, ϕ^B and θ^B followed the motion profiles. At a fixed stroke amplitude ϕ^B_{amp} of 180°, the pitch amplitudes θ^B_{amp} changed within 190° to $-$10° at intervals of 10°. Hence, α in the stroke phase became $-$5° to 95° (21 cases). The wingbeat frequency f was 1/16 s (0.0625 Hz) to maintain the proper range of Re. The sampling frequency was 200 Hz; thus, 3200 samples in a unit wingbeat cycle were acquired.

$$J = \frac{U_\infty}{\overline{U}_{\text{tip}}} = \frac{U_\infty}{2\phi_{\text{amp}} R f} \tag{1}$$

$$\text{Re} = \frac{(\overline{U}_{\text{tip}} + U_\infty)c}{\nu} = \frac{(1+J)(2\phi_{\text{amp}} R f)c}{\nu} \tag{2}$$

As shown in equations (1) and (2), J and Re are functions of f. We selected the seven J cases of 0 (hovering), 0.125, 0.25, 0.5, 0.75, 1.0, and ∞ to cover all forward flight speeds. Re was ~10^4, which corresponds to an adequate flight range of FWMAVs. A fixed value of f brought out slight variation of Re from 1.0 to 2.0 $\times$ 10^4. This range of Re is considerably far from the critical Re (~10^3), as indicated in previous studies [37–44].

Figure 2 also presents the strategy used to avoid the influences of an underdeveloped wake and inertia force that arise due to the sudden departure of the wing. The sequence was briefly composed of three steps, i.e. operation, resting, and rewinding, with the latter including a second rest. During the operation step, the wing motion started from the rest in the middle of the upstroke. The motion was maintained during the wingbeat cycles $T = 2.5$ in the cases of $J \leqslant 0.25$, whereas the operation when $T = 1.5$ was enough to remove the effects when $J > 0.5$ [35]. In the first resting step, the wing was temporarily suspended when $T = 0.5$ for the quiescent flow condition, and the tare weights for this attitude (middle of the downstroke) were collected. The model was then rewound to the initial location for repetition. The data acquired in this step was also used as the tare weights for this attitude (middle of the upstroke). Such sequence sets were repeated 20 times to confirm the repeatability of this apparatus. As shown in figure 2, the raw data sets were analogous to each other, which indirectly imply the suitability of this procedure.

3. Feasibility of the quasi-steady assumption

Figure 3(a) explains the reference points, $r_{2,\text{F}}$ and $r_{2,\text{M}}$, and the reference velocities of U_{ref} and U_{inst} used to acquire the aerodynamic coefficients. First, we employed the conventional BET concept to find the reference points which are functions of the wing planform and the location of the stroke axis (see appendix A for details). U_{ref} and U_{inst} were then derived by considering the relative wind speed at the middle of the stroke and the time-varying inflow speed, respectively, as shown in equations (3) and (4).

$$U_{\text{ref}} = U_{\phi=0} = R\hat{r}_2\dot{\phi}_{\phi=0} - U_\infty \tag{3}$$

$$U_{\text{inst}}(t) = R\hat{r}_2\dot{\phi}(t) - U_\infty \cos\phi(t) \tag{4}$$

Figure 3(b) shows U_{inst} in a unit wingbeat cycle. The wing when hovering ($J = 0$) had a constant U_{inst} due to the constant $\dot{\phi}$ motion profile in the stroke phase.

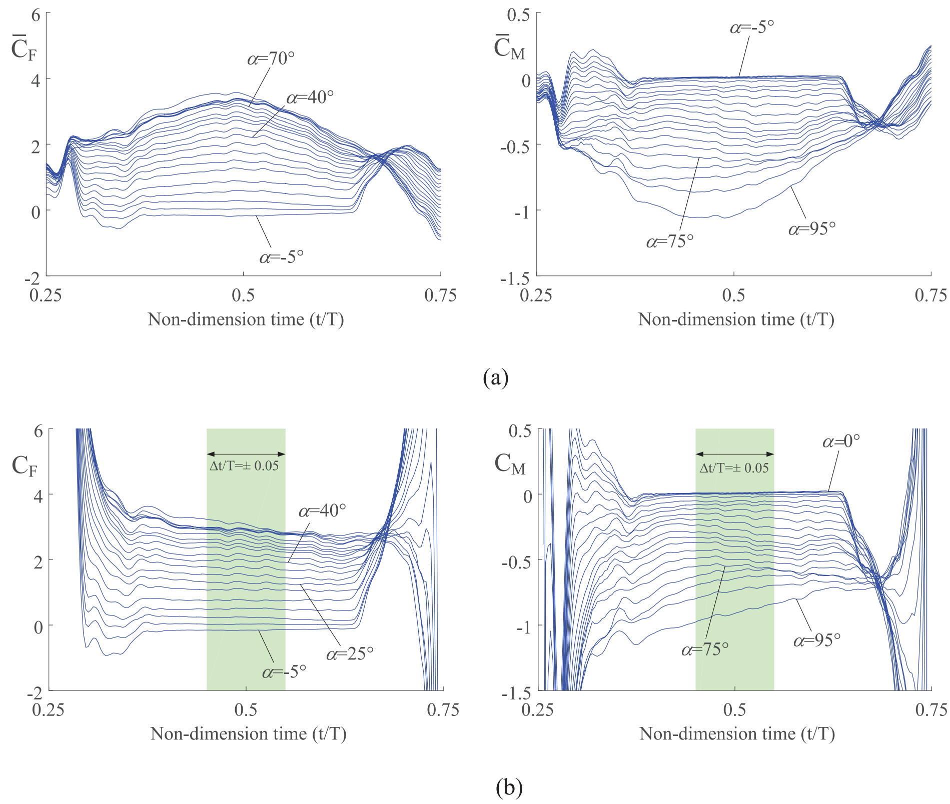

Figure 4. Time-historical values of C_F and C_M when $J = 0.25$. (a) U_{Ref} based $\overline{C}_F$ and $\overline{C}_M$. (b) U_{Inst} based C_F and C_M.

U_{inst} gradually changes as the J increases, and become close to zero in the middle of upstroke when $J = 0.5$. Such a small value of U_{inst} resulted in nearly stagnant movement of the wing and an unreasonable outcome of the aerodynamic coefficients due to the divide-by-zero error. When $J = 1.0$, the reference point was moved forward even during the upstroke owing to the rapid forward speed. This also brought about an opposite angle of attack. As a result, we took the results until $J \geqslant -0.25$ (during the upstroke when $J = 0.25$) into account to build the model.

Figures 4(a) and (b) display the time-historical aerodynamic coefficients when $J = 0.5$ as part of the test of the validity of the quasi-steady assumption. Here, the bar on each coefficient indicates that it is a U_{ref}-based coefficient, as shown in equations (5) and (6).

$$\overline{C}_F = \frac{F_{net}}{\frac{1}{2}\rho U_{ref}^2 S} \quad (5)$$

$$C_F = \frac{F_{net}}{\frac{1}{2}\rho U_{inst}^2 S} \quad (6)$$

$\overline{C}_F$ and $\overline{C}_M$ monotonically increased and gradually took on a sinusoidal shape as α increased. However, C_F and C_M showed nearly constant force and moment production levels during the entire stroke. These production outcomes indicate that the time-historical changes of $\overline{C}_F$ and $\overline{C}_M$ stemmed solely from the relative freestream velocity $U_\infty \cos\phi$, with the unsteadiness negligible in most cases. These findings were consistent for all cases of α, indicating the appropriateness of the quasi-steady assumption at least in this higher range of Re at ~10^4. A linear decrement along the timeline in instances with higher values of α may arise due to the changing-LEV-axial-velocity, as Sun [48] pointed out. A large amplitude of $\phi_{amp}^B = 180\,^\circ$ aggravated this effect, because the wingtip in these moments was heading to the forward direction, and the freestream came from the wingtip. However, such an effect only appears to play a minor role in most cases. Because insects typically use a deep inclined stroke plane for propulsion, and the potential to face the wingtip toward the freestream does not arise. As shown in figure 4(b), it is still negligible near the middle of the stroke. We compiled the results in the shaded region around $\Delta t/T = \pm 0.05$ in the middle of the stroke to build the aerodynamic model.

Figures 5(a)–(c) denote the collected values of $C_L(\alpha)$, $C_D(\alpha)$, and $C_M(\alpha)$ for nine cases of J. As expected, all C_L values show sinusoidal lift curves [5] except for the results at $J = \infty$, which shows the typical aerodynamic characteristics of a low AR flat-plate wing [52]. The peak near $\alpha = 45°$ in the case of $J = 0$ (the thick gray line) is also in accord with the findings in other literatures [31]. One notable feature in C_L is the peak location when trending toward a low α with an increase in J. It drifted widely from $\alpha \sim 55°$ at $J = -0.25$ (the thick blue dashed line) to $\alpha \sim 25°$ at $J = \infty$ (the thin black line). Han *et al* [35] inferred that α may play a substantial role in governing the LEV, equal to the extent of J. They compared to the results of Bross *et al* [53], finding that the LEV on

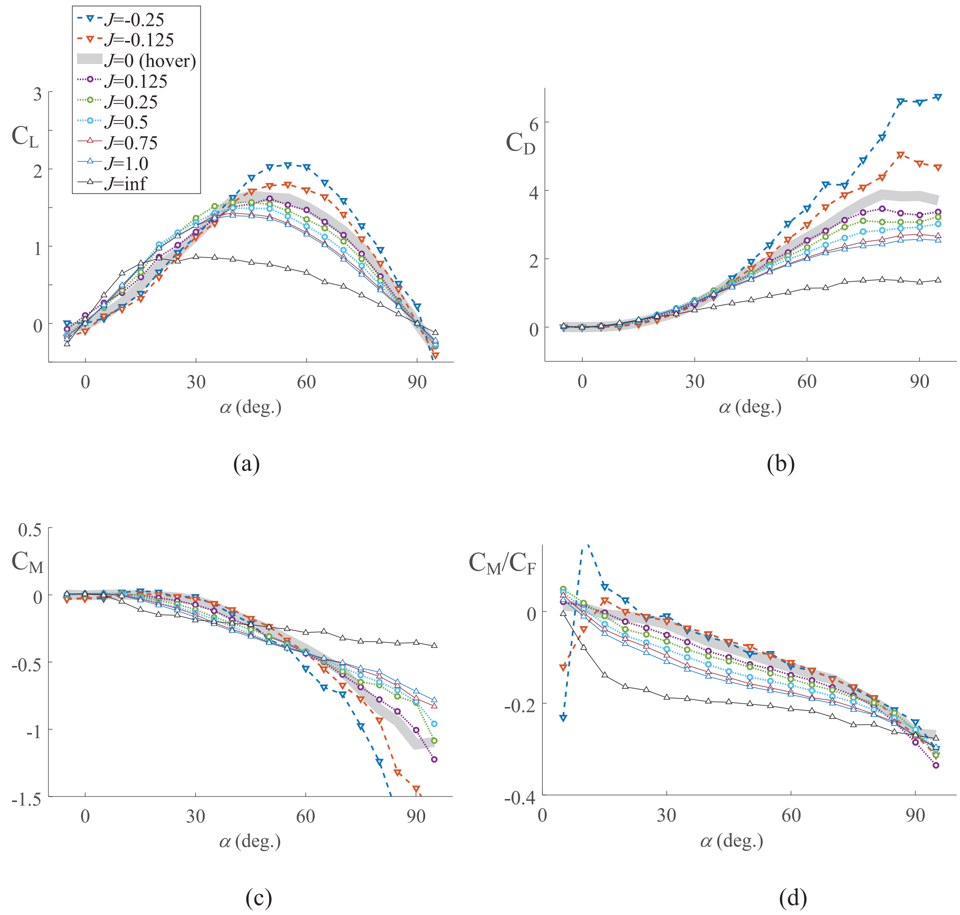

Figure 5. $C_L(\alpha)$, $C_D(\alpha)$, and $C_M(\alpha)$, and the normalized locations of CP in nine J cases as compiled for the aerodynamic models. (a) $C_L(\alpha)$. (b) $C_D(\alpha)$. (c) $C_M(\alpha)$. (d) Normalized locations of CP.

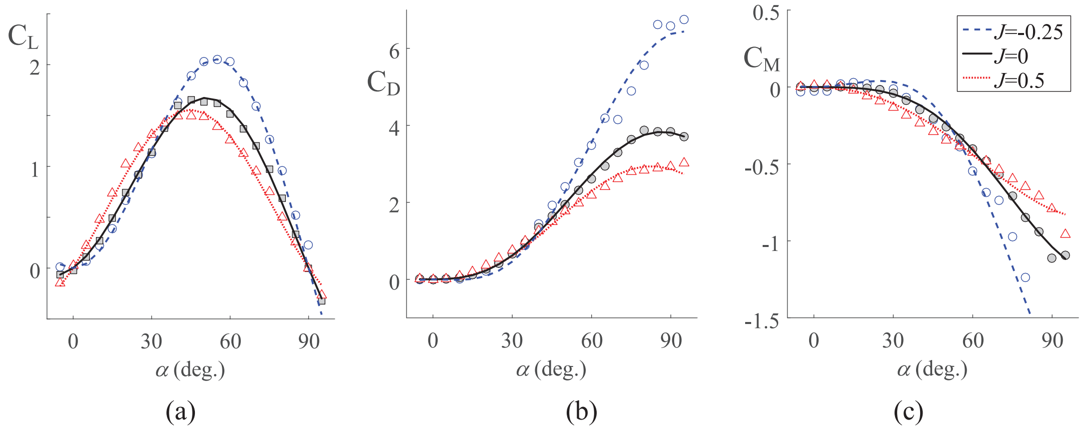

Figure 6. C_L, C_D, and C_M with the regression curves as fit by the Polhamus analogy. (a) $C_L(\alpha)$. (b) $C_D(\alpha)$. (c) $C_M(\alpha)$.

a wing with a lower value of α would be rather stable at higher values of J. Their inference is clearly in line with such wide drift outcomes of the C_L peaks.

Another finding was the substantial lift decrement as J increased. This led to a steady reduction of C_L. C_D was also reduced with an increase in J, which reflected the degraded vortical force caused by the unstable LEV in higher values of J [35].

The effects of J on the characteristics of C_M should be highlighted. Strong pitching-down moment in negative J cases, as observed at high values of α, gradually weakening with an increase in J. When $J = \infty$, a sudden drop in C_M which arose near the stall angle provided indirect evidence of flow separation and stall-like vortex structures [52].

$$C_M/C_F = \frac{M_{Z,\text{wing}}}{\frac{1}{2}\rho U_{\text{inst}}^2 Sc} \bigg/ \frac{F_{X,\text{wing}}}{\frac{1}{2}\rho U_{\text{inst}}^2 S} = \frac{M_Z}{F_X}\frac{1}{c} \tag{7}$$

Figure 5(d) describes the normalized locations of the centers of pressure CP along the chordwise direction (refer to equation (7) for the mathematical description).

As Han et al [31] noted, CP when $J = 0$ gradually moved to $1/2c$, after which there was no noticeable difference in the negative J cases. As J increased, however, CP moved to the trailing edge at an earlier α, and CP at $J = \infty$ was finally fixed at $1/2c$ except for the pre-stall region. With regard to the LEV, which reinforces the adverse pressure near the leading edge, these curves suitably explain the behavior, which is attenuated with an increase in J [35].

4. Devising the aerodynamic force and moment coefficients

Figure 6 shows the regression curves at $J = -0.25$, $J = 0.125$, and $J = 1.0$ as samples to validate the fitness of the curve-fit models. As shown in equations (8)–(10), we borrowed the Polhamus leading-edge suction analogy [24, 25] in order to ensure simplicity and to cover the effects of J, which distorts the curves from a first-order sinusoid. In this analogy, two independent coefficients of K_P and K_V represent the potential and vortex forces, respectively. The C_M model was modified so that it matched the aerodynamic net forces and the location of CP; thus, the $\cos\alpha$ values were removed from the second term. MATLAB® was employed to determine the values of K_P and K_V in finite J cases. All of the R-squares extracted from the curves of C_L, C_D and C_M were higher than 0.992, 0.988, and 0.974, indicating the appropriateness of the regression curves.

$$C_L(\alpha, J) = K_{P,L}(J)\sin(\alpha)\cos^2(\alpha) + K_{V,L}(J)\sin(\alpha)^2\cos(\alpha) \quad (8)$$

$$C_D(\alpha, J) = K_{P,D}(J)\sin(\alpha)^2\cos(\alpha) + K_{V,D}(J)\sin(\alpha)^3 \quad (9)$$

$$C_M(\alpha, J) = K_{P,M}(J)\sin(\alpha)^2\cos(\alpha) + K_{V,M}(J)\sin(\alpha)^2 \quad (10)$$

Equations (12) and (13) are the final forms of the correction factors K_P and K_V for the aerodynamic force and moment models, respectively. Table 1 also presents the sets of coefficients for these K_P and K_V values. We employed power functions to build these factors, as in Lee et al [54]. Using these forms gave us the advantage of being able to adjust both the singular points and converging values for each correction factor. In order to assign the singular points of the factors, for example, we added specific values to the actual J. These values were determined by the ideal case, in which the absolute stroke velocity on the reference point becomes zero. Given this supposition, the aerodynamic forces and moment acting on the surface may be zero. Relying on the definition of J according to equation (1), these values for the forces and moment were finally calculated as $\hat{r}_2$ and $\hat{r}_M$, respectively.

$$K_{P,F \text{ or } V,F} = a(J + \hat{r}_2)^b + d \quad (12)$$

$$K_{P,M \text{ or } V,M} = a(J + \hat{r}_M)^b + d \quad (13)$$

Table 1. Coefficients of the correction factors K_P and K_V.

		a	b	d
Lift	$K_{P,L}$	−2.109	−0.606	4.136
	$K_{V,L}$	2.659	−0.666	−0.344
Drag	$K_{P,D}$	−0.182	−2.414	1.370
	$K_{V,D}$	0.765	−1.497	2.078
Pitching moment	$K_{P,M}$	0.803	−0.972	−0.363
	$K_{P,M}$	−0.242	−1.354	−0.554

Figure 7 shows K_P, K_V, and the regression curves. One interesting feature is that all curves converged as J increased. This clearly indicates both a decrement of the aerodynamic performance [48] as well as the appropriateness of this compensation methodology. The values of K_V depending on J, accounting for the portion of K_P in the low J cases, quantitatively demonstrated the degradation of the vorticity of the LEV and the consequent weak vortex lift during forward flight [35, 45].

In order to consider the rotational force and moment components, we used an approach identical to that in the literature [12, 31]. Equation (14) was utilized to extract the rotational force coefficient C_R, where $\hat{x}_0$ is the non-dimensionalized location of the pitching axis.

$$C_R = \pi(0.75 - \hat{x}_0) \quad (14)$$

The contribution of the added mass on a flapping wing is usually predicted by the inviscid theory [20]. However, this approach is only adequate when the flow is fully attached. Han et al [31] found that an inviscid-based added-mass model was not likely to be compatible in high Re and high α configurations, which introduce intricate wake structures, as indicated in earlier studies [37–44]. Note that an increase in J attenuates the LEV [35]. This implies that a wing in forward flight creates more irregularly shaped wake structures, which cannot be modelled by the conventional aerodynamic model. In order to overcome this issue, DeLaurier [55] employed half of the added mass coefficient for a flapping wing in the post-stall region. This appears to be acceptable because it can be inferred that the attached flow only appears on the pressure side of the wing. The CFD results by Lee et al [54], which show that the correction factor of the added-mass model was <1, would support such an inference.

$$C_A = \pi/8 \quad (15)$$

Equation (15) is the added mass coefficient in the present study, which is half of the theoretical value used by DeLaurier [55]. We used this coefficient for the added-mass model with the simplified description proposed by Troung et al [56] (refer to appendix B for details).

5. Results and discussion

Figures 8(a) and (b) display the time-historical lift, drag, and wing pitching moment in the cases of $J = 0.5$ and $J = 1.0$. In these cases, the wing follows artificial wing kinematics of the type widely employed

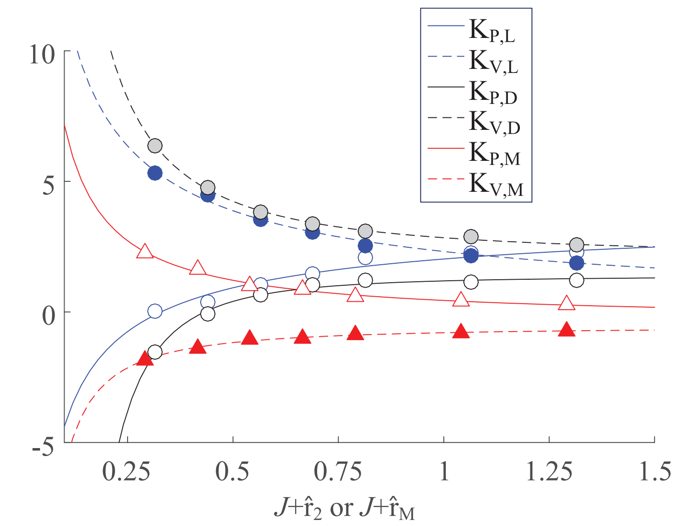

Figure 7. Final forms of the correction factors K_P and K_V for the models (power functions).

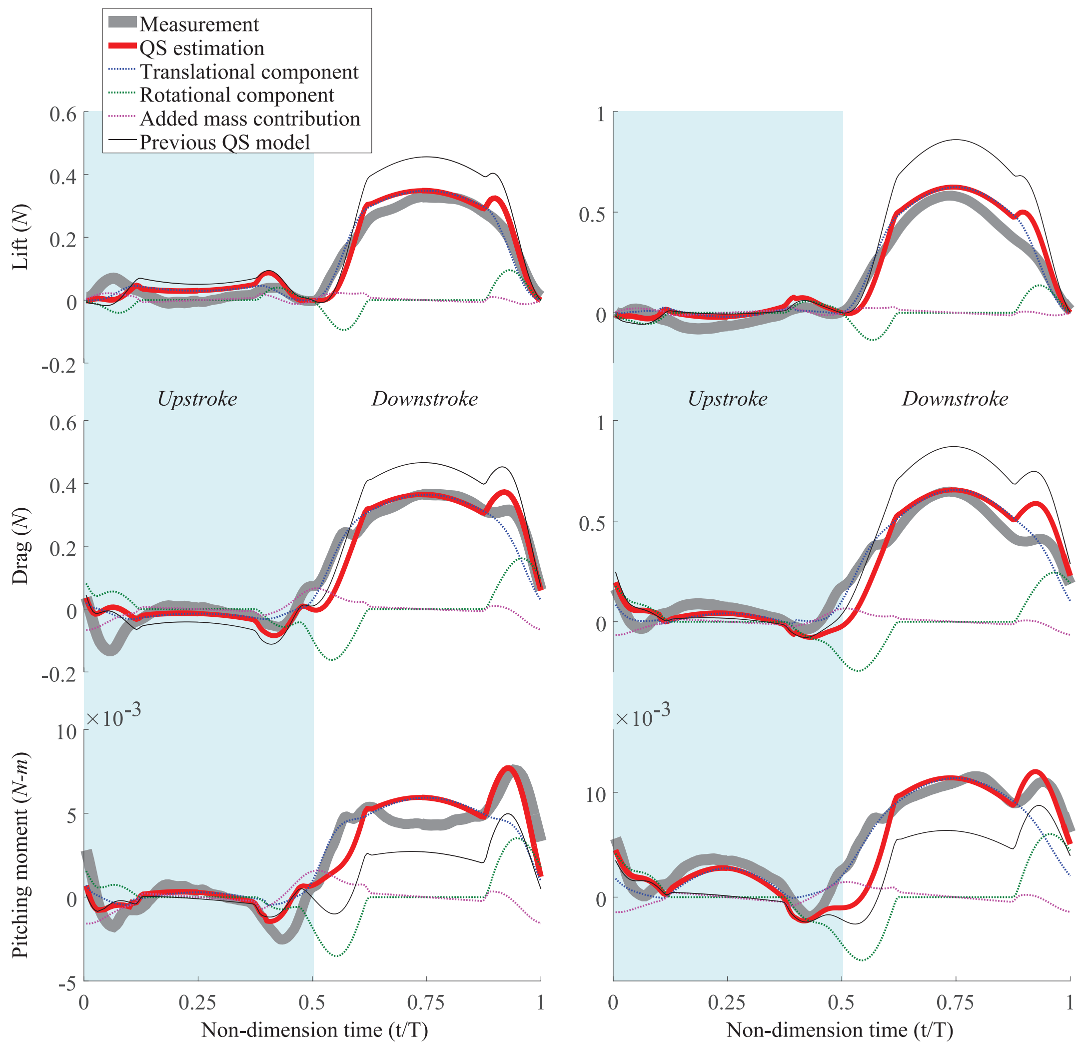

a) b)

Figure 8. The time-historical lift, drag, and wing pitching moment for artificial wingbeat motion. (a) $J = 0.50$. (b) $J = 1.0$.

in previous studies [6, 8, 22]. Borrowing certain notations [22], the wing motion can be expressed as follows: $\phi_{\mathrm{amp}} = 120°$, $\alpha_{\mathrm{amp}} = 90°$, $t/T_{R,\phi} = 0.24$, and $t/T_{R,\alpha} = 0.24$. The previous quasi-steady estimations (the thin black lines) are represented by the hover-based semi-empirical aerodynamic model devised by Han *et al* [31]. In the present model, J was instantaneously calculated and applied to the model at each time step. The border was defined at $J > -0.25$ in order to prevent the extrapolation and divergence of K_P and K_V.

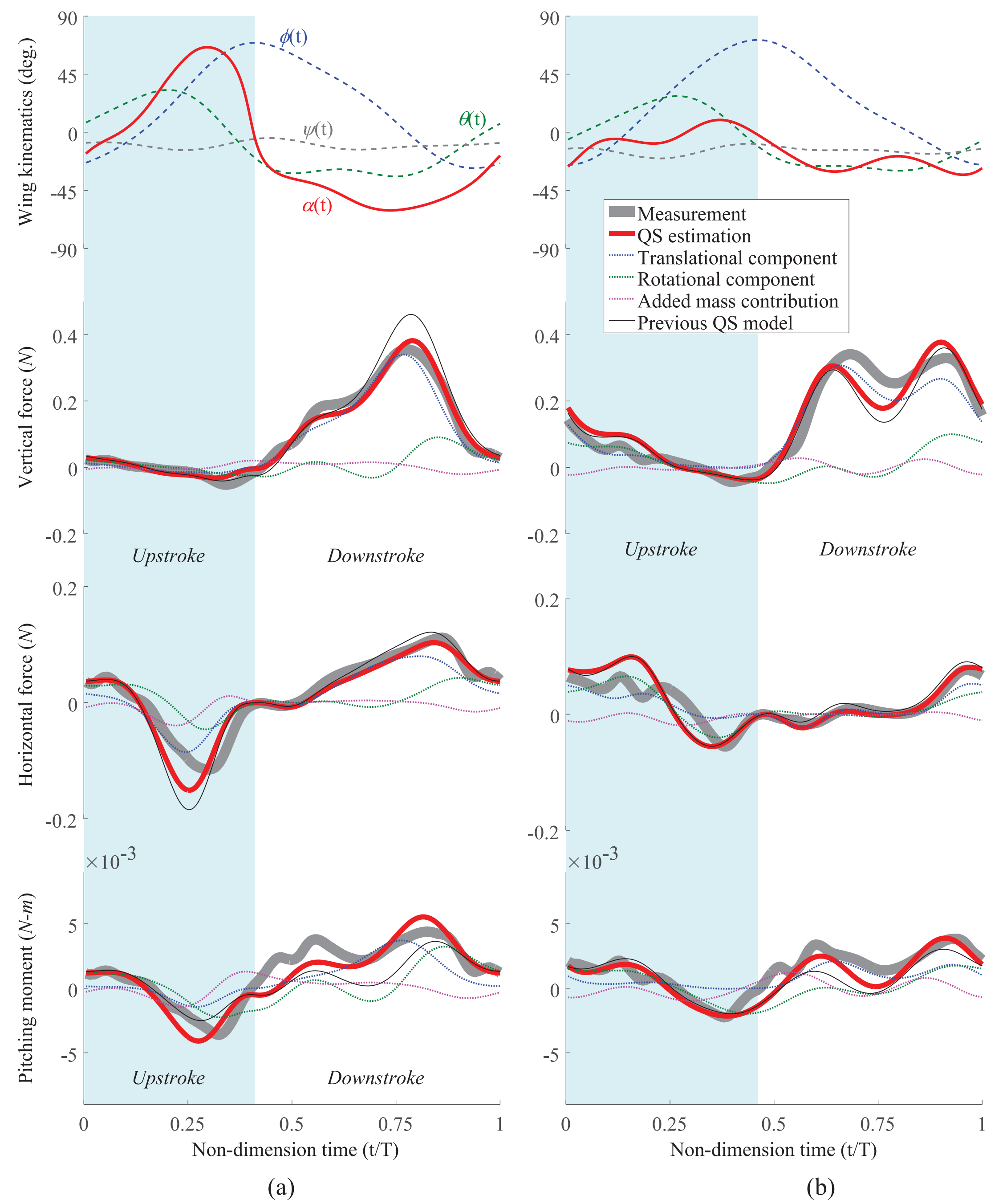

Figure 9. Comparison results in practical cases, as obtained by the wing motions of a living hawkmoth [46]. (a) 2.9 m s^{-1} ($J = 0.63$). (b) 5.0 m s^{-1} ($J = 0.95$). Reproduced with permission of the Journal of Experimental Biology [46].

As shown in figures 8(a) and (b), the present model adequately estimated the time-historical lift and drag in most sections. At the beginning of each stroke, where strong peaks of wing-wake interaction existed in the hovering case, the model appeared to be more accurate, as the wings faced with the freestream could avoid the wake effects, as reported in Han *et al* [35]. However, the reductions of the rotational peaks in the measurements indicated that the simplified rotational force and moment models, based on the Kutta–Joukowski theory [12], should be revised at least for this artificial wingbeat motion.

The previous model (thin black lines) overestimated the lift and drag, which mainly appeared in the downstroke. Note that the increase in J could depress the Coriolis and/or centripetal forces of the flow fields around the wing surface, thereby weakening the vorticity of the LEV and consequently the overall aerodynamic performance [45, 57]. Thus, these types of overestimations are inevitable because the previous aerodynamic model was based on the hovering configuration creating the stable LEV.

The final rows in figures 8(a) and (b) describe the wing pitching moments along the spanwise axis when $J = 0.50$ and $J = 1.0$. The previous moment model (the thin black lines) showed significant underestimations with reference to the measurements, and these were particularly remarkable in the downstroke. The rotational moment component (green dashes) appears to attempt to compensate for the peak immediately before the stroke reversal, but it becomes excessive at $J = 1.0$. This clearly indicates that the previous model is not suitable for use to estimate the aerodynamic moment on the

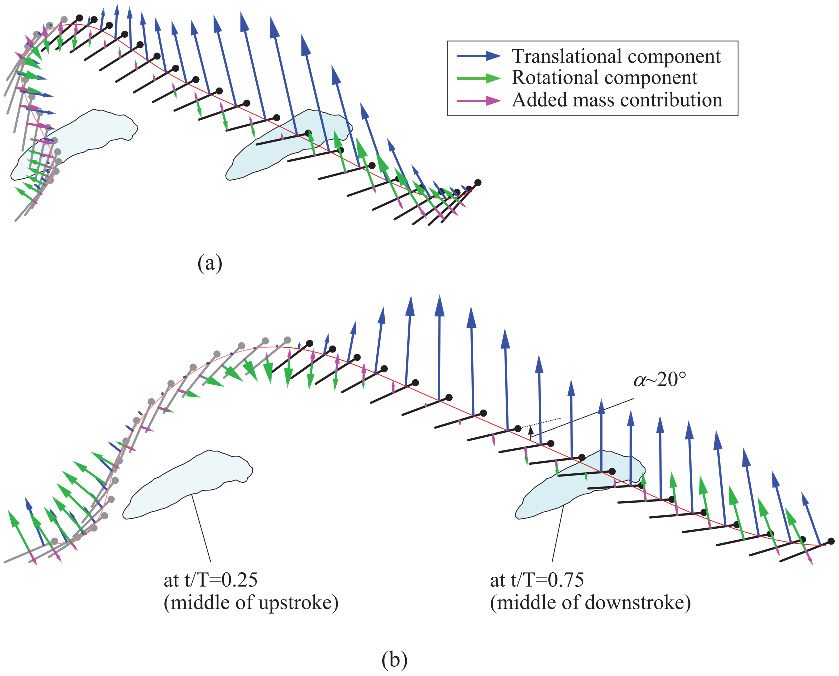

Figure 10. Schematics of the time-varying force components during forward flight. (a) 2.9 m s^{-1} ($J = 0.63$). (b) 5.0 m s^{-1} ($J = 0.95$).

wing during forward flight. In contrast, each of the time-historical estimations by the present model (red thick lines) compensated for these effects and was in good agreement with the measurements. There was slight gap at the stroke reversals in $J = 0.5$, but it had mostly disappeared at $J = 1.0$. One noticeable outcome is the estimation capabilities during the upstroke in both cases, signifying that using the instantaneous J to calculate the pitching moment is reasonable. This arises because the present model employed a negative value of J to yield C_M in this phase. As Han *et al* [31] pointed out, the pitching moment is directly associated with longitudinal flight stability. This clearly indicates that the flight stability and control analysis relying on the previous aerodynamic model should be reinterpreted by the present model or other models that can encompass the effects of J [48].

One remaining issue associated with these types of aerodynamic models is the actual performances for practical configurations. The wing in this configuration had fully 3D motion depending on the circumstances. In order to move forward, for example, the wing employs additional kinematics such as a deep inclined stroke plane β. Aerodynamic models in these situations may diverge from the quasi-steady assumption and therefore provide inaccurate estimations of the aerodynamic force, moment, and trim condition which form the baseline of flight stability and control analyses.

In order to validate the model, we chose the wing-beat motion of a hawkmoth at forward speeds of 2.9 and 5.0 m s^{-1} [46], which correspond to the preferred flight speed [39] and the maximum flight speed. The wing kinematics of $\phi(\mathrm{t})$, $\theta(\mathrm{t})$, and $\psi(\mathrm{t})$ were extracted from the literature [46] and were curve-fit with a third-order Fourier series. Here, $\theta(\mathrm{t})$ is the mean value of all of the cross-sections in the literature [46], and the stroke plane angles β were constant at 44.4° and 56.3°, respectively.

Figures 9(a) and (b) display the comparison results in practical cases. The graphs in the first row show the kinematics with $\alpha(\mathrm{t})$, where $\alpha(\mathrm{t})$ is the chord line angle from the inflow vector at the reference point (refer to appendix B for details). In both cases, the values of $\alpha(\mathrm{t})$ were comparably distorted from $\theta(\mathrm{t})$. Note the curves during the downstroke; $\alpha(\mathrm{t})$ at 2.9 m s^{-1} was augmented to over 45°, whereas $\alpha(\mathrm{t})$ in the case of 5.0 m s^{-1} was instead reduced. With regard to the freestream, however, both wing kinematics appears adequately to reflect each trim condition. At a flight speed of 2.9 m s^{-1}, the lift only produced by the downstroke would be sufficient to keep the body aloft owing to the inflow velocity. On the other hand, the wing at 5.0 m s^{-1} would attempt to reduce the drag using a low α rather than producing more lift, as the lift in this configuration is strong enough due to the massive inflow.

The mean values in the 2.9 m s^{-1} case (the preferred flight speed) were compared with the trim condition in order to validate such inferences. The present aerodynamic model estimated the mean body lift (vertical force) and drag (horizontal force) as 0.109 and 0.0075N, respectively. Given the relationship between the scaled-up model and an actual insect determined by Fry *et al* [58], the lift and drag were converted to 1.974 g and 0.136 g. These numbers clearly indicated the trim conditions (the weight of the hawkmoth was 1.995 g [46]) and the capability of the present aerodynamic model, which can provide accurate results even in practical cases.

The time-historical lift and drag (correspondingly the second and third rows in figure 10) also support the appropriateness of the present model. The time-historical changes were in fairly good agreement with the measurements, only showing slight differences of 1.8% and 6.6% from the measurements of the mean lift values. In contrast to the results from the present model, the previous aerodynamic model did not compensate for the effects of J, thereby yielding excessive lift estimations of 12% and 29% in the downstroke phase (the thin black lines in the second row). The drag at both flight speeds also drifted from the measurements. Regarding the pitching moments, the previous model estimated lower values at certain temporal locations.

One advantage of this type of aerodynamic model is that the force and moment can easily be decomposed into the translational, rotational, and added-mass components. Note that these components were individually governed by the α, $\dot{\alpha}$, and $\ddot{\alpha}$, implying that we can very conveniently evaluate the wingbeat motion and predict which component is dominant when generating lift, thrust, and counteract moment in each stroke phase. In addition, an evaluation with living insects can offer information about how insects use their wings to gain flight stability, which would be helpful for designing flapping actuators and motion profiles of FWMAVs in detail.

We found that most of the lift was produced by the translational component, and was solely distributed in the downstroke at both speeds (figure 10). These components accounted for 87.2% and 83.0% in the total lift production. The rotational components only accounted for 12.5% and 7.8%, and the added mass only had portions of 0.65% and 1.73% in the total lift. These rotational and added-mass components are much lower than those of a hovering fruit fly, playing a substantial role in lift production (~35% in the total lift production) [5]. In order words, translational force component may be enough by itself to generate lift in forward flight.

Another notable feature is that the values of α, which gradually decreased with respect to an increase in J, were likely to be associated with each maximum value of C_L. This variation in α can not only be observed on the wings of fruit flies [59], which have a stroke plane of nearly zero and which use asymmetric pitching motions for free-flight maneuvers [60], but also on other insects [61] which directly tilt the mean force vector using an inclined stroke plane. In the case of a hawkmoth [46], the α reconstructed from the kinematics varied from ~50° at 0.9 m s^{-1} to ~10° at 5.0 m s^{-1} near the middle of the downstroke. Note the distribution of the peaks of C_L, as shown in figure 5(a). This change of α with respect to J is fairly coincident with the maximum values of C_L. This implies that insects may use an optimal α to generate lift depending on the circumstances.

We also found that the rotational components during pronation ($0.2 < t/T < 0.4$ at 2.9 m s^{-1}; $0.26 < t/T < 0.46$ at 5.0 m s^{-1}) had a remarkable role in the generation of thrust. These accounted for 22.6% and 75.0%. The added mass also contributed to thrust generation at 13.0% and 45.8% at forward speeds of 2.9 and 5.0 m s^{-1}. The total portion of ~121% at 5.0 m s^{-1} should be noted. This indicates that the translational component could not generate any thrust at this speed, while the rotational and added-mass components must be employed to eliminate the drag and to maintain this high-speed forward flight.

The rapid wing pitch during pronation also led to strong pitching-down moment near the end of the upstroke. These pitching-down moments counteract to cancel each other out, with the pitching-up moment likely accumulating when the wing produces lift during the downstroke. We inferred that an insect may use the rapid wing pitch for the trim, and the rotational moment components are essential to generate the pitching-down moment. As stated above, the rotational components were solely governed by the pitch rate. This clearly indicates that the wing pitch mechanism should be considered with $\dot{\alpha}$ and $\ddot{\alpha}$ in order to improve the performance capabilities of FWMAVs.

6. Conclusion

In order to allow a model to predict accurate aerodynamic forces and moment during a forward flight configuration, the aerodynamic characteristics depending on α and J in 147 individual cases were collected and interpreted. The Polhamus leading-edge suction analogy was then employed, and the power functions were used to build the correction factors K_P and K_V. All K_P and K_V values converged as J increased, indicating both the attenuation of the aerodynamic performances and the feasibility of the compensation strategy used in the present study. The increase in K_P and the degradation of K_V with respect to J, which describe LEV attenuation and the weakened vortex lift, were also in line with earlier works on the effects of J on a flapping wing. While the previous model over- or underestimated the aerodynamic forces and moment, this model clearly showed adequate estimations. The model also showed better estimations than those by the previous model in practical cases. In particular, the present model brought a noticeable improvement in the aerodynamic pitching moment estimation capability, even when the wing had fully 3D motion. This model indicated that a smaller α during the downstroke may be adequate to generate lift during high-speed forward flight. Moreover, the rotational and added-mass components during the upstroke played a substantial role in producing the thrust and in maintaining the body pitch. The proposed model can contribute to determining the design requirements of FWMAVs, including the detailed wingbeat motion profiles, and can provide the basis for analyzing the flight stability, control, and dynamic characteristics of living insects and FWMAVs during forward flight.

Acknowledgments

This work was supported by a grant from the National Research Foundation of Korea (NRF) funded by the Korean government (MSIP) (No. NRF-2016R1A6A3A11931608).

Appendix A. The geometric parameters for the BET

This chapter derives BET-based geometrical parameters of flapping wings. This would help readers understand definitions that require the additional parameters of r_2 and r_M. Figure A1 shows a schematic of the blade elements and major reference quantities. Here,

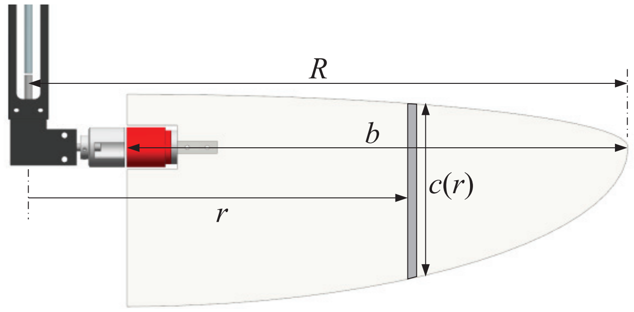

Figure A1. Geometry of the model wing.

R denotes the pivot-based geometric parameters. Reconstruction starts from the typical Euler number, which is expressed as the surface area and velocity square. In the case of hovering, this number can be rewritten as equations (A.1) and (A.2) using the locations of the blade elements and the related integration.

$$F = \sum_{\mathrm{ele}=1}^{N} C_{\mathrm{F}}\frac{1}{2}\rho U_{\mathrm{ele}}^2 \cdot c_{\mathrm{ele}}(r)\cdot \Delta r = \int_0^R C_{\mathrm{F}}\frac{1}{2}\rho(\dot{\phi}r)^2 c(r)\cdot \mathrm{d}r = C_{\mathrm{F}}\frac{1}{2}\rho\dot{\phi}^2\int_0^R r^2 c(r)\cdot \mathrm{d}r \quad \text{(A.1)}$$

Using the normalized lengths of $\hat{c}$ and $\hat{r}$, we obtain the following integral quantities,

$$F = C_{\mathrm{F}}\frac{1}{2}\rho\dot{\phi}^2\int_0^1(\hat{r}R)^2\hat{c}\bar{c}R\cdot \mathrm{d}\hat{r} = C_{\mathrm{F}}\frac{1}{2}\rho\dot{\phi}^2R^3\bar{c}\int_0^1\hat{r}^2\hat{c}\cdot \mathrm{d}\hat{r} = C_{\mathrm{F}}\frac{1}{2}\rho U_{\mathrm{Tip}}^2 S\cdot\hat{r}_2^2,$$

where

$$\hat{r}_2^2 = \int_0^1\hat{r}^2\hat{c}\cdot \mathrm{d}\hat{r}$$

is the non-dimensional second moment of the wing area. (A.2)

Likewise,

$$M = \sum_{\mathrm{ele}=1}^{N} C_{\mathrm{M}}\frac{1}{2}\rho U_{\mathrm{ele}}^2\cdot c_{\mathrm{ele}}^2(r)\cdot\Delta r = \int_0^R C_{\mathrm{M}}\frac{1}{2}\rho(\dot{\phi}r)^2c^2\cdot \mathrm{d}r = C_{\mathrm{M}}\frac{1}{2}\rho\dot{\phi}^2\int_0^R r^2c^2\cdot \mathrm{d}r \quad \text{(A.3)}$$

$$M = C_{\mathrm{M}}\frac{1}{2}\rho\dot{\phi}^2\int_0^1(\hat{r}R)^2(\hat{c}\bar{c})^2R\cdot \mathrm{d}\hat{r} = C_{\mathrm{M}}\frac{1}{2}\rho\dot{\phi}^2R^3\bar{c}^2\int_0^1\hat{r}^2\hat{c}^2\cdot \mathrm{d}\hat{r} = C_{\mathrm{M}}\frac{1}{2}\rho U_{\mathrm{Tip}}^2S\bar{c}\cdot\hat{r}_{\mathrm{M}}^2$$

$$\hat{r}_{\mathrm{M}}^2 = \int_0^1\hat{r}^2\hat{c}^2\cdot \mathrm{d}\hat{r} \quad \text{(A.4)}$$

The simple process above clearly indicates the necessity of $\hat{r}_2$ and $\hat{r}_{\mathrm{M}}$ as the reference points for flapping wing aerodynamics and implies that $U_{\mathrm{Ref}} = U_{\mathrm{tip}}\cdot\hat{r}_2$ is more suitable as the reference velocity to express the aerodynamic characteristics of biological flyers, as empirically found by Lua *et al* [47].

For the wing with a horizontal stroke plane in forward flight, $U_{\mathrm{ele}} = \dot{\phi}r + U_\infty\cos\phi$. The integration term in equation (A.1) is then written as follows:

$$F = C_{\mathrm{F}}\frac{1}{2}\rho\int_0^R[(\dot{\phi}r)^2 + 2\dot{\phi}rU_\infty\cos\phi + (U_\infty\cos\phi)^2]c(r)\cdot \mathrm{d}r$$

$$= C_{\mathrm{F}}\frac{1}{2}\rho\left[\underbrace{\int_0^R\dot{\phi}^2r^2c(r)\cdot \mathrm{d}r}_{(1)} + \underbrace{\int_0^R 2\dot{\phi}rU_\infty\cos\phi c(r)\cdot \mathrm{d}r}_{(2)} + \underbrace{\int_0^R U_\infty^2\cos^2\phi c(r)\cdot \mathrm{d}r}_{(3)}\right]$$

$$(1) = \int_0^1\dot{\phi}^2\hat{r}^2R^3\hat{c}\bar{c}\cdot \mathrm{d}\hat{r} = U_{\mathrm{Tip}}^2S\cdot\hat{r}_2^2$$

$$(2) = 2\dot{\phi}U_\infty\cos\phi\int_0^1\hat{r}R^2\hat{c}\bar{c}\cdot \mathrm{d}\hat{r} = 2U_{\mathrm{Tip}}U_\infty S\cdot\hat{r}_1^1$$

$$(3) = U_\infty^2\cos^2\phi\cdot S\int_0^1\bar{c}\cdot \mathrm{d}\hat{r} = U_\infty^2\cos^2\phi\cdot S$$

Employing the tip velocity ratio μ from the study by Dickson and Dickinson [32] results in

$$F = C_{\mathrm{F}}\frac{1}{2}\rho[U_{\mathrm{Tip}}^2\hat{r}_2^2 + 2U_{\mathrm{Tip}}U_\infty\cos\phi\hat{r}_1^1 + U_\infty^2\cos^2\phi]S = C_{\mathrm{F}}\frac{1}{2}\rho U_{\mathrm{Tip}}^2[\hat{r}_2^2 + 2\mu\hat{r}_1^1 + \mu^2]S. \quad \text{(A.5)}$$

Here,

$$\mu = \frac{U_\infty(\mathrm{t})}{U_{\mathrm{Tip}}} = \frac{U_\infty\cos\phi}{\dot{\phi}R}, \text{ and}$$

$$\hat{r}_1^1 = \int_0^1\hat{r}\hat{c}\cdot \mathrm{d}\hat{r}: \text{ the non-dimensional first moment of the wing area.} \quad \text{(A.6)}$$

Meanwhile, the reference point-based description becomes

$$F = C_{\mathrm{F}}\frac{1}{2}\rho(U_{\mathrm{Tip}}\hat{r}_2 + U_\infty\cos\phi)^2S = C_{\mathrm{F}}\frac{1}{2}\rho U_{\mathrm{Tip}}^2[\hat{r}_2^2 + 2\mu\hat{r}_2^2 + \mu^2]S. \quad \text{(A.7)}$$

Although equation (A.5) is theoretically adequate for the BET in forward flight, we used equation (A.7) to determine C_{F} and C_{M}, as derived from the fixed reference point. In fact, the $\hat{r}_2^2$ and $\hat{r}_1^1$ combination in equation (A.5) offers the moving reference point depending on J. This implies that the interpretation

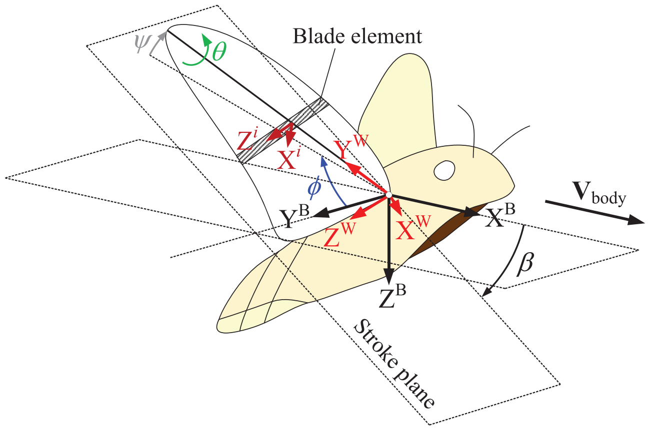

Figure B1. The schematic of the body- and wing-fixed frames, and the kinematic definitions.

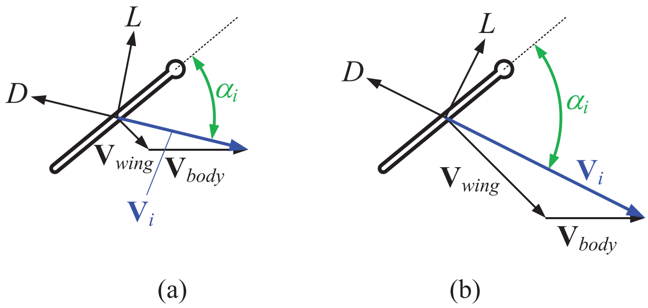

Figure B2. The values of α_i and $\mathbf{V}_i$ at the in- and outboard blade elements. (a) Inboard section. (b) Outboard section.

of the effect of J would be somewhat flawed due to its movement. In contrast, using equation (A.7) gave us a simple and more intuitive sense. This is also how power functions are utilized to build correction factors, which are functions of $\hat{r}_2$. When considering the potential of readers who must use the present aerodynamic model to design FWMAVs, using equation (A.7) is much easier when determining the wing planform, and it yields a proper reference point regardless of a change in the forward speed. In our calculation, there were only slight differences between them. In the case of $J = 0.25$, for example, the maximum difference was $<3\%$.

Appendix B. Mathematical description of the aerodynamic model

Figure B1 describes two different frames on the wing and the body and the relationship between the wing kinematics. These utilize the notation used in Willmott and Ellington [46]. Due to this notation, the stroke plane angle β and deviation angle ψ should show a negative rotating direction in Euler angles, and these were included in equation (B.1).

Figure B2 shows the schematics of the angles of attack and the directions of the translational lift and drag components on the inboard and outboard blade elements. In contrast to hovering flight, which does not have a freestream, the angles of attack on each blade element vary with the spanwise location and are gradually distributed on the wing. This implies that the magnitudes of the angles of attack and the directions of the lift and drag should be individually calculated with respect to the inflow vectors (the sum of $\mathbf{V}_{\text{wing}}$ and $\mathbf{V}_{\text{body}}$), and applying a vector relationship may provide an easier description of the aerodynamic model.

The Euler angle from the body-fixed frame to the wing-fixed frame $\mathrm{R}^{\mathrm{B}\to\mathrm{W}}$ could be derived using the following equation (B.1), where the superscripts B and W denote the body- and wing-fixed frames, respectively.

$$\mathrm{R}^{\mathrm{B}\to\mathrm{W}} = \mathrm{R}_\theta \mathrm{R}_\psi \mathrm{R}_\phi \mathrm{R}_\beta$$

$$\text{Here, } \mathrm{R}_\theta = \begin{bmatrix} \cos\theta & 0 & -\sin\theta \\ 0 & 1 & 0 \\ \sin\theta & 0 & \cos\theta \end{bmatrix}, \ \mathrm{R}_\psi = \begin{bmatrix} 1 & 0 & 0 \\ 0 & \cos\psi & -\sin\psi \\ 0 & \sin\psi & \cos\psi \end{bmatrix}, \mathrm{R}_\phi = \begin{bmatrix} \cos\phi & \sin\phi & 0 \\ -\sin\phi & \cos\phi & 0 \\ 0 & 0 & 1 \end{bmatrix},$$

$$\text{and } \mathrm{R}_\beta = \begin{bmatrix} \cos\beta & 0 & \sin\beta \\ 0 & 1 & 0 \\ -\sin\beta & 0 & \cos\beta \end{bmatrix}. \tag{B.1}$$

Using the above descriptions, the forward velocity of the body in the body-fixed frame $\mathbf{V}^{\mathrm{B}}_{\mathrm{body}}$ could be transformed to the wing-fixed frame, as shown in equation (B.2).

$$\mathbf{V}^{\mathrm{W}}_{\mathrm{body}} = \mathbf{R}^{\mathrm{B}\rightarrow\mathrm{W}}\mathbf{V}^{\mathrm{B}}_{\mathrm{body}} \tag{B.2}$$

The angular velocity of the wing in the wing-fixed frame can be expressed by equation (B.3), as $\dot{\phi}$, $\dot{\psi}$, and $\dot{\theta}$ are defined with respect to the first, second, and third destinations of $\mathbf{R}^{\mathrm{B}\rightarrow\mathrm{W}}$.

$$\boldsymbol{\omega}^{\mathrm{W}}_{wing} = \begin{bmatrix}0\\ \dot{\theta}\\ 0\end{bmatrix} + \mathbf{R}_{\theta}\begin{bmatrix}\dot{\psi}\\ 0\\ 0\end{bmatrix} + \mathbf{R}_{\theta}\mathbf{R}_{\psi}\begin{bmatrix}0\\ 0\\ \dot{\phi}\end{bmatrix}. \tag{B.3}$$

Equation (B.4) expresses the inflow velocity vector on the ith blade element $\mathbf{V}^{\mathrm{W}}_{i,\mathrm{inflow}}$, where $\mathbf{r}^{\mathrm{W}}_i$ denotes the distance from the pivot to the ith blade and only has a y-component. $\mathbf{V}^{\mathrm{W}}_i$ shown in equation (B.5) is the final version of $\mathbf{V}^{\mathrm{W}}_{i,\mathrm{inflow}}$ for the BET, where the y-component of $\mathbf{V}^{\mathrm{W}}_{i,\mathrm{inflow}}$ is eliminated as the BET is based on two dimensions.

$$\mathbf{V}^{\mathrm{W}}_{i,\mathrm{inflow}} = \mathbf{V}^{\mathrm{W}}_{\mathrm{body}} + \boldsymbol{\omega}^{\mathrm{W}}_{\mathrm{wing}} \times \mathbf{r}^{\mathrm{W}}_i \tag{B.4}$$

$$\mathbf{V}^{\mathrm{W}}_i = \begin{bmatrix}1 & 0 & 0\\ 0 & 0 & 0\\ 0 & 0 & 1\end{bmatrix}\mathbf{V}^{\mathrm{W}}_{\mathrm{inflow}} \tag{B.5}$$

In order to calculate the angle of attack of the ith blade α_i, we defined another unit vector lying on the ith blade element $\hat{\mathbf{c}}^{\mathrm{W}}_i$, which is heading to the leading edge. Subsequently, α_i becomes the angle between the two vectors. It can be determined by equation (B.6),

$$\alpha_i = \tan^{-1}\frac{\sqrt{[\mathbf{V}^{\mathrm{W}}_i \times \hat{\mathbf{c}}^{\mathrm{W}}_i]^T[\mathbf{V}^{\mathrm{W}}_i \times \hat{\mathbf{c}}^{\mathrm{W}}_i]}}{\mathbf{V}^{\mathrm{W}}_i\cdot\hat{\mathbf{c}}^{\mathrm{W}}_i}, \tag{B.6}$$

$$\text{where } \hat{\mathbf{c}}^{\mathrm{W}}_i = [0 \quad 0 \quad -1]^T.$$

The direction cosine matrices on the blade elements were also pre-defined for the directions of the translational lift and drag components. Here, the first term of $\hat{\mathbf{l}}^{\mathrm{W}}_i$ denotes the sign for the lift direction with respect to the x-component of the inflow vector $\mathbf{V}^{\mathrm{W}}_i$. All of the y-components are invalid with this procedure.

$$\hat{\mathbf{l}}^{\mathrm{W}}_i = \frac{\mathbf{V}^{\mathrm{W}}_i\cdot i^{\mathrm{W}}_i}{\sqrt{(\mathbf{V}^{\mathrm{W}}_i\cdot i^{\mathrm{W}}_i)(\mathbf{V}^{\mathrm{W}}_i\cdot i^{\mathrm{W}}_i)}}\begin{bmatrix}0 & 0 & 1\\ 0 & 1 & 0\\ -1 & 0 & 0\end{bmatrix}\frac{\mathbf{V}^{\mathrm{W}}_i}{\sqrt{[\mathbf{V}^{\mathrm{W}}_i]^T\mathbf{V}^{\mathrm{W}}_i}}$$

$$\hat{\mathbf{d}}^{\mathrm{W}}_i = \begin{bmatrix}-1 & 0 & 0\\ 0 & 0 & 0\\ 0 & 0 & -1\end{bmatrix}\frac{\mathbf{V}^{\mathrm{W}}_i}{\sqrt{[\mathbf{V}^{\mathrm{W}}_i]^T\mathbf{V}^{\mathrm{W}}_i}}.$$

The acceleration of the blade elements $\mathbf{a}^{\mathrm{W}}_i$ for estimating the added-mass contribution was derived from the alternative version of $\mathbf{V}^{\mathrm{W}}_{i,\mathrm{inflow}}$, as it should be described as the acceleration of each center of the blade element [56]. Thus, $\mathbf{s}^{\mathrm{W}}_i = [0 \quad \mathbf{r}^{\mathrm{W}}_i\cdot\hat{j}^{\mathrm{W}} \quad c^*_i]^T$.

$$\mathbf{a}^{\mathrm{W}}_{i,\mathrm{inflow}} = \frac{\mathrm{d}}{\mathrm{d}t}\mathbf{V}^{\mathrm{W}}_{\mathrm{inflow}@c^*_i} = \frac{\mathrm{d}}{\mathrm{d}t}\mathbf{R}^{\mathrm{B}\rightarrow\mathrm{W}}\mathbf{V}^{\mathrm{B}}_{\mathrm{body}} + \underbrace{\cancel{\mathbf{R}^{\mathrm{B}\rightarrow\mathrm{W}}\frac{\mathrm{d}}{\mathrm{d}t}\mathbf{V}^{\mathrm{B}}_{\mathrm{body}}}}_{\substack{\text{if a=0}\\ \text{(uniform speed)}}} + \frac{\mathrm{d}}{\mathrm{d}t}\boldsymbol{\omega}^{\mathrm{W}}_{\mathrm{wing}} \times \mathbf{s}^{\mathrm{W}}_i + \underbrace{\cancel{\boldsymbol{\omega}^{\mathrm{W}}_{\mathrm{wing}} \times \frac{\mathrm{d}}{\mathrm{d}t}\mathbf{s}^{\mathrm{W}}_i}}_{\mathbf{s}^{\mathrm{W}}_i=\text{const.}}$$

$$= \frac{d}{dt}\mathbf{R}^{\mathrm{B}\rightarrow\mathrm{W}}\mathbf{V}^{\mathrm{B}}_{body} + \frac{d}{dt}\boldsymbol{\omega}^{\mathrm{W}}_{wing} \times \mathbf{s}^{\mathrm{W}}_i. \tag{B.7}$$

The derivatives of the combination of the Euler angle are as follows:

$$\frac{\mathrm{d}}{\mathrm{d}t}\mathbf{R}^{\mathrm{B}\rightarrow\mathrm{W}} = \frac{\mathrm{d}}{\mathrm{d}t}\mathbf{R}_{\theta}\mathbf{R}_{\psi}\mathbf{R}_{\phi}\mathbf{R}_{\beta} + \mathbf{R}_{\theta}\frac{d}{dt}\mathbf{R}_{\psi}\mathbf{R}_{\phi}\mathbf{R}_{\beta} + \mathbf{R}_{\theta}\mathbf{R}_{\psi}\frac{\mathrm{d}}{\mathrm{d}t}\mathbf{R}_{\phi}\mathbf{R}_{\beta} + \mathbf{R}_{\theta}\mathbf{R}_{\psi}\mathbf{R}_{\phi}\frac{\mathrm{d}}{\mathrm{d}t}\mathbf{R}_{\beta}$$

$$\frac{\mathrm{d}}{\mathrm{d}t}\boldsymbol{\omega}^{\mathrm{W}}_{\mathrm{wing}} = \begin{bmatrix}0\\ \ddot{\theta}\\ 0\end{bmatrix} + \frac{\mathrm{d}}{\mathrm{d}t}\mathbf{R}_{\theta}\begin{bmatrix}\dot{\psi}\\ 0\\ 0\end{bmatrix} + \mathbf{R}_{\theta}\begin{bmatrix}\ddot{\psi}\\ 0\\ 0\end{bmatrix} + \frac{\mathrm{d}}{\mathrm{d}t}\mathbf{R}_{\theta}\mathbf{R}_{\psi}\begin{bmatrix}0\\ 0\\ \dot{\phi}\end{bmatrix} + \mathbf{R}_{\theta}\frac{\mathrm{d}}{\mathrm{d}t}\mathbf{R}_{\psi}\begin{bmatrix}0\\ 0\\ \dot{\phi}\end{bmatrix} + \mathbf{R}_{\theta}\mathbf{R}_{\psi}\begin{bmatrix}0\\ 0\\ \ddot{\phi}\end{bmatrix}.$$

Equations (B.8) and (B.9) are the final forms of the present aerodynamic model, where the subscripts of trans, rot, and added denote the translational, rotational, and added-mass components. All of the following formulas in the curved brackets yield scalar values, and the following unit vectors assign the direction at the wing-fixed frame.

$$\mathbf{F}^{\mathrm{W}} = \mathbf{F}^{\mathrm{W}}_{\mathrm{trans}} + \mathbf{F}^{\mathrm{W}}_{\mathrm{rot}} + \mathbf{F}^{\mathrm{W}}_{\mathrm{added}} \tag{B.8}$$

$$\mathbf{M}^{\mathrm{W}} = \mathbf{M}^{\mathrm{W}}_{\mathrm{trans}} + \mathbf{M}^{\mathrm{W}}_{\mathrm{rot}} + \mathbf{M}^{\mathrm{W}}_{\mathrm{added}} \tag{B.9}$$

Here, $\mathbf{F}^{\mathrm{W}}_{\mathrm{trans}} = \sum_{i=1}^{N}\left\{C_{\mathrm{L}}\frac{1}{2}\rho[\mathbf{V}^{\mathrm{W}}_i]^T\mathbf{V}^{\mathrm{W}}_i c_i\Delta r\right\}\hat{\mathbf{l}}^{\mathrm{W}}_i$

$$+ \sum_{i=1}^{N}\left\{C_{\mathrm{D}}\frac{1}{2}\rho[\mathbf{V}^{\mathrm{W}}_i]^T\mathbf{V}^{\mathrm{W}}_i c_i\Delta r\right\}\hat{\mathbf{d}}^{\mathrm{W}}_i$$

$$\mathbf{F}^{\mathrm{W}}_{\mathrm{rot}} = \sum_{i=1}^{N}\left\{C_{\mathrm{R}}\rho(\boldsymbol{\omega}^{\mathrm{W}}_{wing}\cdot\hat{j}^{\mathrm{W}})\sqrt{[\mathbf{V}^{\mathrm{W}}_i]^T\mathbf{V}^{\mathrm{W}}_i}\,c_i^2\Delta r\right\}\hat{i}^{\mathrm{W}}$$

$$\mathbf{F}^{\mathrm{W}}_{\mathrm{added}} = \sum_{i=1}^{N}\{C_{\mathrm{A}}\rho(\mathbf{a}^{\mathrm{W}}_i\cdot\hat{i}^{\mathrm{W}})c_i^2\Delta r\}\hat{i}^{\mathrm{W}}$$

$$\mathbf{M}^{\mathrm{W}}_{\mathrm{trans}} = \sum_{i=1}^{N} \left\{ C_{\mathrm{M}} \frac{1}{2} \rho [\mathbf{V}_i^{\mathrm{W}}]^T \, \mathbf{V}_i^{\mathrm{W}} c_i^2 \Delta r \right\} \hat{j}^{\mathrm{W}} + \sum_{i=1}^{N} \{ \mathbf{r}_i^{\mathrm{W}} \times \mathbf{F}^{\mathrm{W}}_{i,\mathrm{trans}} \}$$

$$\mathbf{M}^{\mathrm{W}}_{\mathrm{rot}} = \sum_{i=1}^{N} \{ \mathbf{s}_i^{\mathrm{W}} \times \mathbf{F}^{\mathrm{W}}_{i,\mathrm{rot}} \}$$

$$\mathbf{M}^{\mathrm{W}}_{\mathrm{added}} = \sum_{i=1}^{N} \{ \mathbf{s}_i^{\mathrm{W}} \times \mathbf{F}^{\mathrm{W}}_{i,\mathrm{added}} \}.$$

The inverse Euler angle can be used to transform to the body-fixed frame, as follows:

$$\mathbf{F}^{\mathrm{B}} = [\mathbf{R}^{\mathrm{B}\rightarrow\mathrm{W}}]^T \, \mathbf{F}^{\mathrm{W}}$$

$$\mathbf{M}^{\mathrm{B}} = [\mathbf{R}^{\mathrm{B}\rightarrow\mathrm{W}}]^T \, \mathbf{M}^{\mathrm{W}}:$$

the moments at the pivot in figure B1.

References

[1] Shyy W, Aono H, Kang C-k and Liu H 2013 *An introduction to Flapping Wing Aerodynamics* (Cambridge: Cambridge University Press)
[2] Chin D D and Lentink D 2016 Flapping wing aerodynamics: from insects to vertebrates *J. Exp. Biol.* **219** 920–32
[3] Ellington C P, van den Berg C, Willmott A P and Thomas A L R 1996 Leading-edge vortices in insect flight *Nature* **384** 626–30
[4] Sane S P 2003 The aerodynamics of insect flight *J. Exp. Biol.* **206** 4191–208
[5] Dickinson M H, Lehmann F O and Sane S P 1999 Wing rotation and the aerodynamic basis of insect flight *Science* **284** 1954–60
[6] Sun M and Tang J 2002 Unsteady aerodynamic force generation by a model fruit fly wing in flapping motion *J. Exp. Biol.* **205** 55–70
[7] Birch J M and Dickinson M H 2003 The influence of wing-wake interactions on the production of aerodynamic forces in flapping flight *J. Exp. Biol.* **206** 2257–72
[8] Wu J H and Sun M 2005 The influence of the wake of a flapping wing on the production of aerodynamic forces *Acta Mech. Sin.* **21** 411–8
[9] Lu H, Lua K B, Lim T T and Yeo K S 2016 Ground effect on the aerodynamics of three-dimensional hovering wings *Bioinspiration Biomimetics* **11** 066003
[10] Lua K B, Lee Y J, Lim T T and Yeo K S 2016 Aerodynamic effects of elevating motion on hovering rigid hawkmoth-like wings *Am. Inst. Aeronaut. Astronaut. J.* **54** 2247–64
[11] Lim T T, Teo C J, Lua K B and Yeo K S 2009 On the prolong attachment of leading edge vortex on a flapping wing *Mod. Phys. Lett.* B **23** 357–60
[12] Sane S P and Dickinson M H 2002 The aerodynamic effects of wing rotation and a revised quasi-steady model of flapping flight *J. Exp. Biol.* **205** 1087–96
[13] Taha H E, Hajj M R and Nayfeh A H 2012 Flight dynamics and control of flapping-wing MAVs: a review *Nonlinear Dyn.* **70** 907–39
[14] Faruque I and Humbert J S 2010 Dipteran insect flight dynamics. Part 1 Longitudinal motion about hover *J. Theor. Biol.* **264** 538–52
[15] Kim J-K, Han J-S, Lee J-S and Han J H 2015 Hovering and forward flight of the hawkmoth *Manduca sexta*: trim search and 6-DOF dynamic stability characterization *Bioinspiration Biomimetics* **10** 056012
[16] Kim J-K, Lee J-S and Han J-H 2012 Passive longitudinal stability in ornithopter flight *J. Guid. Control Dyn.* **35** 669–73
[17] Kim D-K, Lee J-S and Han J-H 2011 Improved aerodynamic model for efficient analysis of flapping-wing flight *Am. Inst. Aeronaut. Astronaut J.* **49** 868–72
[18] Pfeiffer A-T, Lee J-S, Han J-H and Baier H 2010 Ornithopter flight simulation based on flexible multi-body dynamics *J. Bionic Eng.* **7** 102–11
[19] Ellington C 1984 The aerodynamics of hovering insect flight. I. The quasi-steady analysis *Phil. Trans. R. Soc.* B **305** 1–15
[20] Sedov L I, Chu C, Cohen H, Seckler B and Gillis J 1965 Two-dimensional problems in hydrodynamics and aerodynamics *Phys. Today* **18** 62
[21] Kweon J and Choi H 2010 Sectional lift coefficient of a flapping wing in hovering motion *Phys. Fluids* **22** 071703
[22] Han J-S, Chang J W, Kim J-K and Han J-H 2015 Role of trailing-edge vortices on the hawkmoth-like flapping wing *J. Aircr.* **52** 1256–66
[23] Ansari S A, Żbikowski R and Knowles K 2006 Aerodynamic modelling of insect-like flapping flight for micro air vehicles *Prog. Aerosp. Sci.* **42** 129–72
[24] Polhamus E C 1971 Predictions of vortex-lift characteristics by a leading-edge suction analogy *J. Aircr.* **8** 193–9
[25] Traub L W 2004 Analysis and estimation of the lift components of hovering insects *J. Aircr.* **41** 284–9
[26] Pedersen C and Żbikowski R 2006 An indicial-Polhamus aerodynamic model of insect-like flapping wings in hover *Flow Phenom. Nat.* **2** 606–665
[27] Berman G J and Wang Z J 2007 Energy-minimizing kinematics in hovering insect flight *J. Fluid Mech.* **582** 153–68
[28] Andersen A, Pesavento U and Wang Z J 2005 Unsteady aerodynamics of fluttering and tumbling plates *J. Fluid Mech.* **541** 65–90
[29] Taha H E, Hajj M R and Beran P S 2014 State-space representation of the unsteady aerodynamics of flapping flight *Aerosp. Sci. Technol.* **34** 1–11
[30] Mao S and Du G 2003 Lift and power requirements of hovering insect flight *Acta Mech. Sin.* **19** 458–69
[31] Han J-S, Kim J-K, Chang J W and Han J-H 2015 An improved quasi-steady aerodynamic model for insect wings that considers movement of the center of pressure *Bioinspiration Biomimetics* **10** 046014
[32] Lentink D and Dickinson M H 2009 Biofluiddynamic scaling of flapping, spinning and translating fins and wings *J. Exp. Biol.* **212** 2691–704
[33] Lentink D and Dickinson M H 2009 Rotational accelerations stabilize leading edge vortices on revolving fly wings *J. Exp. Biol.* **212** 2705–19
[34] Han J-S, Chang J W and Cho H-K 2015 Vortices behavior depending on the aspect ratio of an insect-like flapping wing in hover *Exp. Fluids* **56** 1–16
[35] Han J-S, Han J-H and Chang J W 2016 An advance ratio effect on the lift augmentations of an insect-like flapping wing in forward flight *J. Fluid Mech.* **808** 485–510
[36] Dickson W B and Dickinson M H 2004 The effect of advance ratio on the aerodynamics of revolving wings *J. Exp. Biol.* **207** 4269–81
[37] Birch J M, Dickson W B and Dickinson M H 2004 Force production and flow structure of the leading edge vortex on flapping wings at high and low Reynolds numbers *J. Exp. Biol.* **207** 1063–72
[38] Lu Y, Shen G X and Lai G J 2006 Dual leading-edge vortices on flapping wings *J. Exp. Biol.* **20** 5005–16
[39] Johansson L C, Engel S, Kelber A, Heerenbrink M K and Hedenstrom A 2013 Multiple leading edge vortices of unexpected strength in freely flying hawkmoth *Sci. Rep.* **3** 3264
[40] Garmann D J, Visbal M R and Orkwis P D 2013 Three-dimensional flow structure and aerodynamic loading on a revolving wing *Phys. Fluids* **25** 034101
[41] Harbig R R, Sheridan J and Thompson M C 2013 Reynolds number and aspect ratio effects on the leading-edge vortex for rotating insect wing planforms *J. Fluid Mech.* **717** 166–92
[42] Kim D and Gharib M 2010 Experimental study of three-dimensional vortex structures in translating and rotating plates *Exp. Fluids* **49** 329–39

[43] Zhang C, Hedrick T L and Mittal R 2015 Centripetal acceleration reaction: an effective and robust mechanism for flapping flight in insects *PLoS One* **10** e0132093
[44] Bross M and Rockwell D 2014 Flow structure on a simultaneously pitching and rotating wing *J. Fluid Mech.* **756** 354–83
[45] Han J-S, Han J-H and Chang J W 2016 Effects of advance ratio on the aerodynamic characteristics of an insect wing in forward flight *AIAA Atmospheric Flight Mechanics Conf.* p 0018
[46] Willmott A P and Ellington C P 1997 The mechanics of flight in the hawkmoth Manduca sexta. I. Kinematics of hovering and forward flight *J. Exp. Biol.* **200** 2705–22
[47] Willmott A P and Ellington C P 1997 The mechanics of flight in the hawkmoth Manduca sexta. II. Aerodynamic consequences of kinematic and morphological variation *J. Exp. Biol.* **200** 2723–45
[48] Sun M 2014 Insect flight dynamics: stability and control *Rev. Mod. Phys.* **86** 615–46
[49] Lua K B, Lai K C, Lim T T and Yeo K S 2010 On the aerodynamic characteristics of hovering rigid and flexible hawkmoth-like wings *Exp. Fluids* **49** 1263–91
[50] Park H and Choi H 2012 Kinematic control of aerodynamic forces on an inclined flapping wing with asymmetric strokes *Bioinspiration Biomimetics* **7** 016008
[51] Lua K B, Lim T T and Yeo K S 2014 Scaling of aerodynamic forces of three-dimensional flapping wings *Am. Inst. Aeronaut. Astronaut J.* **52** 1095–101
[52] Taira K and Colonius T 2009 Three-dimensional flows around low-aspect-ratio flat-plate wings at low Reynolds numbers *J. Fluid Mech.* **623** 187–207
[53] Bross M, Ozen C and Rockwell D 2013 Flow structure on a rotating wing: effect of steady incident flow *Phys. Fluids* **25** 081901
[54] Lee Y J, Lua K B, Lim T T and Yeo K S 2016 A quasi-steady aerodynamic model for flapping flight with improved adaptability *Bioinspiration Biomimetics* **11** 036005
[55] DeLaurier J D 1993 An aerodynamic model for flapping-wing flight *Aeronaut. J.* **97** 125–30
[56] Troung Q T, Nguyen Q V, Troung V T, Park H C, Byun D Y and Goo N S 2011 A modified blade element theory for estimation of forces generated by a beetle-mimicking flapping wing system *Bioinspiration Biomimetics* **6** 036008
[57] Harbig R R, Sheridan J and Thompson M C 2014 The role of advance ratio and aspect ratio in determining leading-edge vortex stability for flapping flight *J. Fluid Mech.* **751** 71–105
[58] Fry S N, Sayaman R and Dickinson M H 2005 The aerodynamics of hovering flight in Drosophila *J. Exp. Biol.* **208** 2303–18
[59] Fry S N, Sayaman R and Dickinson M H 2003 The aerodynamics of free-flight maneuvers in drosophila *Science* **300** 495–8
[60] Ristroph L, Bergou A J, Guckenheimer J, Wang Z J and Cohen I 2011 Paddling mode of forward flight in insects *Phys. Rev. Lett.* **106** 178103
[61] Ellington C P 1999 The novel aerodynamics of insect flight: applications to micro-air vehicles *J. Exp. Biol.* **202** 3439–48